

Corrective Measures to Restore Corrosion Resistance Following Friction Stir Welding

Final Report
2002 - 2004
Rockwell Scientific
Thousand Oaks, CA 91360

Prepared for
Office on Naval Research

BACKGROUND

Friction stir welding (FSW) is a solid state joining process invented at TWI in 1991. This technology makes it possible to join aluminum alloys, which are difficult or impossible to weld by conventional techniques.(1-7) A schematic illustration of the FSW process is shown in Figure 1. To friction stir weld either a butt or lap joint, a specially designed cylindrical tool is rotated and plunged into the joint line. The tool has a small diameter entry probe with a concentric larger diameter shoulder. When descended to the part, the rotating entry probe contacts the surface and rapidly friction heats and softens a small column of metal. As the probe penetrates beneath the surface, part of this metal column is extruded above the surface. The tool shoulder and length of probe control the depth of penetration.

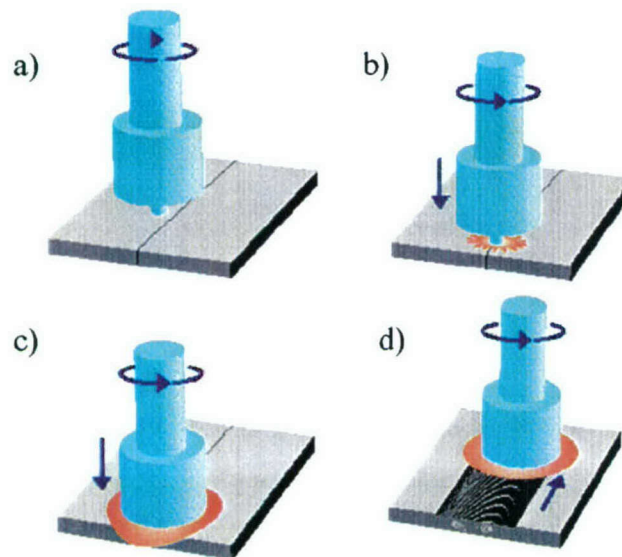


Fig. 1. Schematic illustration of friction stir welding: a) rotating tool prior to contact with the plate; b) tool pin makes contact with the plate, creating heat; c) shoulder makes contact, restricting further penetration while expanding the hot zone; and d) plate moves relative to the rotating tool, creating a fully recrystallized, fine grain microstructure.

DISTRIBUTION STATEMENT A
Approved for Public Release
Distribution Unlimited

When the shoulder contacts the metal surface, its rotation creates additional frictional heat and heat via shear deformation helping to plasticize a larger cylindrical metal column around the inserted probe. The shoulder provides a forging force that contains the upward metal flow caused by the tool probe. During welding, the metals to be joined and the tool are moved relative to each other such that the tool tracks the weld interface. The rotating tool provides a continual hot working action, plasticizing metal within a narrow zone.

Although melting does not occur during FSW, temperatures are sufficiently high and times at temperature are long enough to cause dissolution, nucleation, and/or coarsening of the strengthening precipitates of high strength aluminum alloys. The temperature-time profile changes with distance from the nugget creating gradients in both microstructure and precipitate morphology. Work in the previous ONR program (N00014-99-C-0153) found that FSW sensitizes microstructures in the weld zone of some high strength aluminum alloys. Specifically the aluminum alloys investigated have been AA7050, AA7075, and AA2024. The sensitized regions are more susceptible to stress corrosion cracking (SCC), pitting, and intergranular corrosion than the parent material. Work in the N00014-99-C-0153) identified the severity and location of the attack resulting from the sensitized microstructure neither of which can be predicted from the properties of the parent alloy.(8-10)

The present program (N00014-02-C-0212) has investigated five different approaches to corrective measures that either produce less sensitization or restore the corrosion resistance: 1) Active cooling during FSW, where cold water is circulated through the anvil and a mist of water is sprayed on the tool. This is a process change, which lowers the maximum temperature and decreases the time at elevated temperature. 2) Laser surface melting where surface melting and rapid quenching alters the microstructure, 3) low plasticity burnishing, where a tool puts compressive stresses in a surface layer, 4) pre & post weld heat treatments which homogenizes the grain boundary chemistry, and 5) change in tool design which alters the temperature/time profile and microstructure during FSW. Only tool design and heat treatment had an effect on the corrosion properties. (11-13)

APPROACH

Corrosion Resistance Evaluation

Susceptibility to IGA was determined using a 10% dilution of the ASTM G-34 exfoliation corrosion (EXCO) test solution. The EXCO solution consists of 4 M NaCl, 0.5 M KNO₃, and 0.1 M HNO₃. Test samples approximately 1 cm wide were cut transverse to the weld, exposing cross-sections of the FSW, and were polished with emery paper to 600 grit prior to exposure. The test samples were immersed in the modified EXCO solution for varying time intervals and subsequently examined by optical microscopy.

Susceptibility to SCC was evaluated using the SSR method described in ASTM Standards G-129 and G-49. Tensile specimens were machined transverse to the weld

with the gauge section perpendicular to the rolling direction. Gage cross section dimensions were 6.35 mm x 3.18 mm. The gauge length included the weld nugget and both HAZ's. Specimens were mounted in a 1.5 liter cell and electrically insulated from the grips. Figure 2 shows a sample schematic. A 0.6 M NaCl solution open to the air was continuously recirculated through the cell from a 5 liter reservoir. For comparison, tests were performed in dry laboratory air by placing specimens in plastic tubing packed with anhydrous CaSO_4 (DrieriteTM).

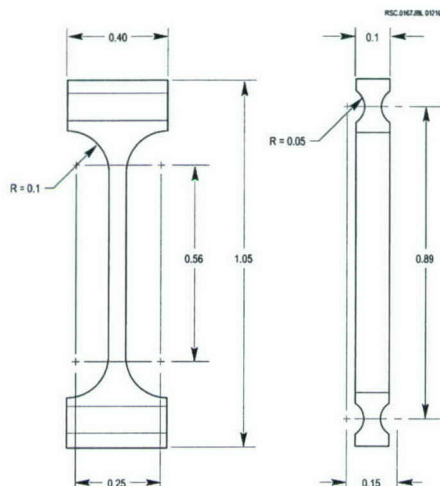


Figure 2. Schematic of SSR test specimen.

TEM Measurements

Thin foils for transmission electron microscopy (TEM) were made from cross-sectional samples taken from the center of the nugget, on both sides of the boundary between nugget and PRZ, and in the base metal. Foils were made using the procedure reported by others for analytical transmission microscopy studies on 7075 and 2024.(14) The weldments were polished metallographically and etched to locate nugget and heat affected zones. A thin slice (~0.6 mm) of the entire cross section was then cut using a slow-speed saw. Circular (3 mm) blanks, centered on the areas of interest, were electro-discharge machined from the slices. The blanks were then mechanically thinned to a thickness of ~0.1 mm prior to electropolishing in a solution of 25% HNO_3 in methanol cooled to -40°C .

Local chemistries of grain interiors and grain boundaries were evaluated using a Philips CM30 transmission electron microscope equipped with a Noran Voyager x-ray energy dispersive spectroscopy (EDS) system. Measurements were made with the probe placed directly over the area of interest and with a beam size of approximately 4 nm. The beam spreads as it passes through the thin-foil specimen, resulting in a spatial resolution on the order of 40 nm. Grain boundary and grain interior compositions were measured between precipitate particles. Compositions are reported as atomic percents. Each value reported is the average of 3 to 6 measurements, and \pm values reflect the maximum deviation from the mean in those measurements.

PROGRESS

Tool design

We examined the effects of tool design as well as the effects of the travel speed of the tool on loss of corrosion resistance of FSW aluminum alloys. Tool design affects the heat input and microstructure, both of which can be important to the SCC properties. The general features of a weld in FSW Al are shown in Figure 3. The FSW region is composed of a nugget, a thermo-mechanically affect zone (TMAZ) and a heat affected zone (HAZ). The nugget is at the center of the processed region and undergoes dynamic recrystallization, having recrystallized equiaxed grains ranging in size from 0.5 μm to 8 μm . The TMAZ is located just outside the weld nugget and undergoes both mechanical deformation and thermal processing. The HAZ is located beyond the TMAZ and has a microstructure that has been modified only by the thermal transient. In the schematic shown in Figure 3, the direction of travel of the tool is out of the plane of the paper. A pronounced shoulder on the nugget distinguishes the advancing side (the side where the tangential rotating tool velocity opposes the travel velocity) from the retreating side. A

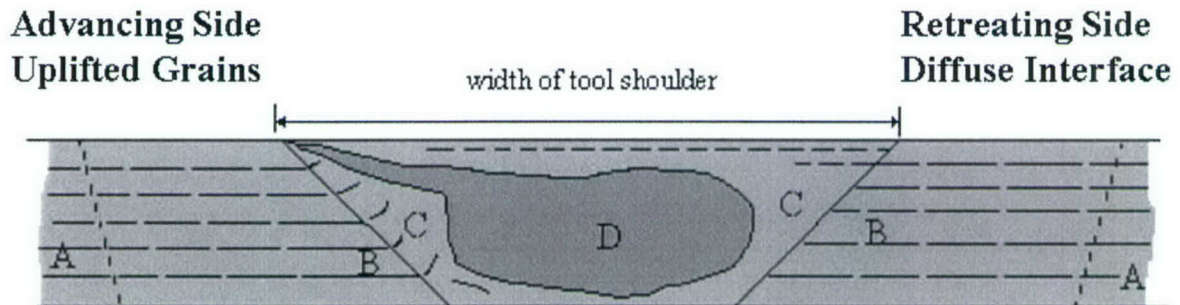


Figure 3. Schematic diagram showing the processed zones in a transverse section of a generic weld region, where the direction of travel of the tool is out the plane of the cross sectional view: A) parent material, B) HAZ, C) TMAZ, and D) Nugget

Three tool geometries (Figure 4) were used to join $\frac{1}{4}$ inch plates of AA 7050-T7651. These were the conventional tool, which has a flat shoulder with a tri-flat threaded pin, a scroll shoulder tool with a tri-flat threaded pin, and a flat shoulder tool with a tri-flute pin. Three different travel speeds were used with the conventional tool and the scroll shoulder tool. The effects of tool design and travel speed on heat input was assessed by temperature measurements made using sheathed thermocouples inserted into the aluminum test plates in line with the FSW tool, and at varying distances from the join line. Typical temperature transients are shown in Figure 5. These transients were recorded using the convention tool at a travel speed of four inches per minute. Arrows indicate the temperatures for the T6 and T7 temper treatments. At the top of the transients, is the location of the thermocouple relative to the join line. The data show that temperatures are above the T6 and T7 tempering temperature for approximately 40

seconds well over 3 cm from the centerline of the weld. Figure 6 is a plot of the maximum temperature (average of two runs) recorded from thermocouples located 6.3 and 7.6 mm from the weld centerline for the scroll shoulder and the conventional tool. The peak temperatures for the conventional tool are significantly higher than those for the scroll shoulder tool at equal distances from the centerline. Also the temperatures on the advancing side are higher than those on the retreating side. Figure 7 shows the maximum temperature (average of two runs) for 2, 4, and 8 ipm travel speeds of the conventional tool at 2 and 3 mm from the centerline. The temperatures are higher on the advancing side and increase with decreasing travel speed.

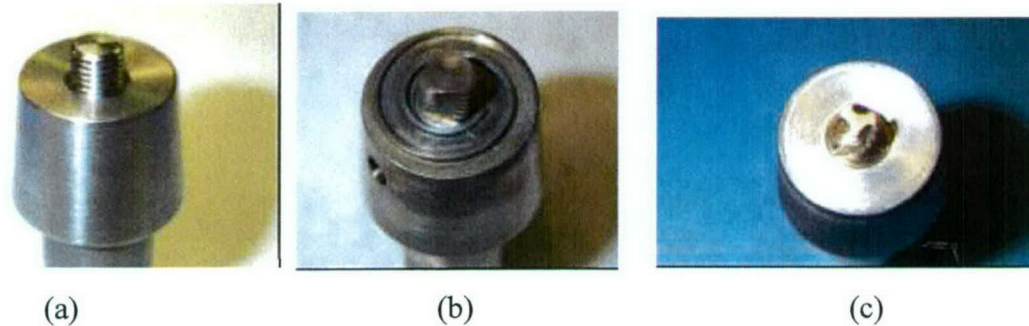


Figure 4. Tool geometries used (a) standard tool, (b) scroll shoulder with a tri-flat threaded pin tool, (c) tri-flute with a tri-flat threaded pin and with a flat shoulder tool.

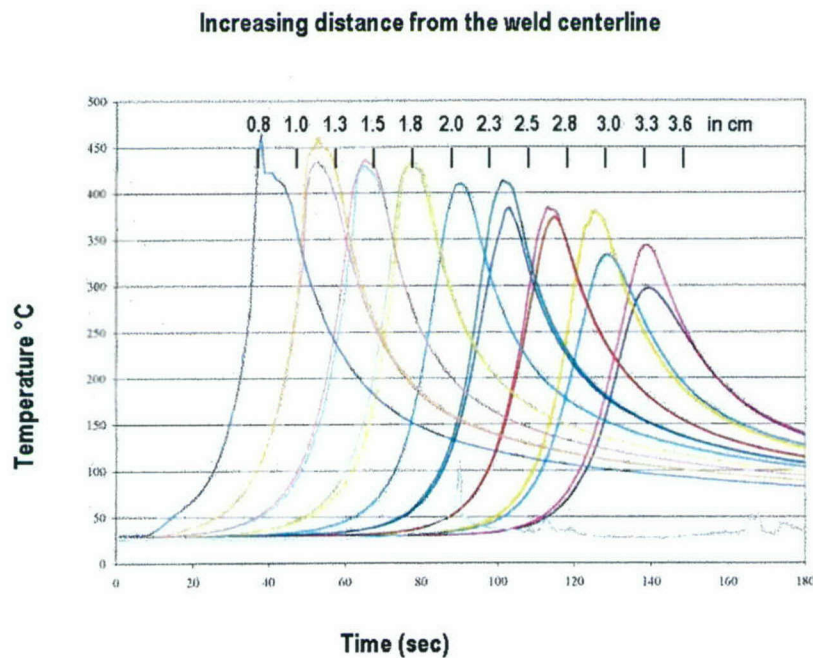


Figure 5. Typical temperature transients (conventional tool, 4 ipm).

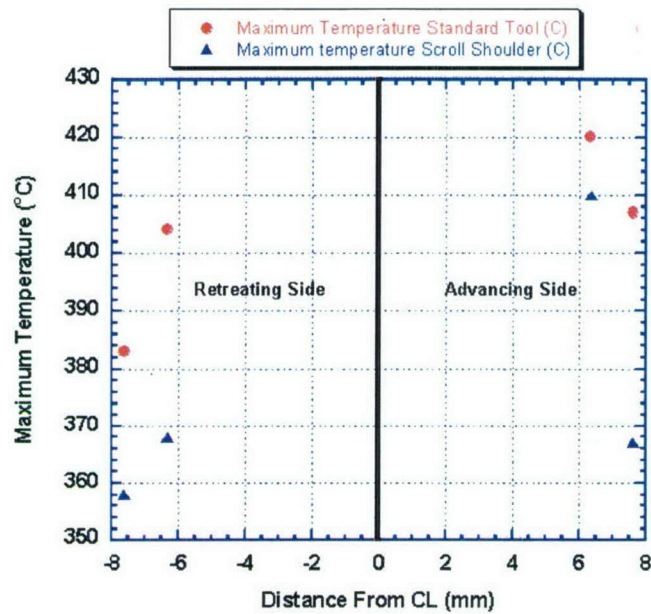


Figure 6. Mean maximum temperature (average of two measurements) recorded during FSW using a standard tool and a scroll shoulder tool. The travel speed was 4 inches per minute.

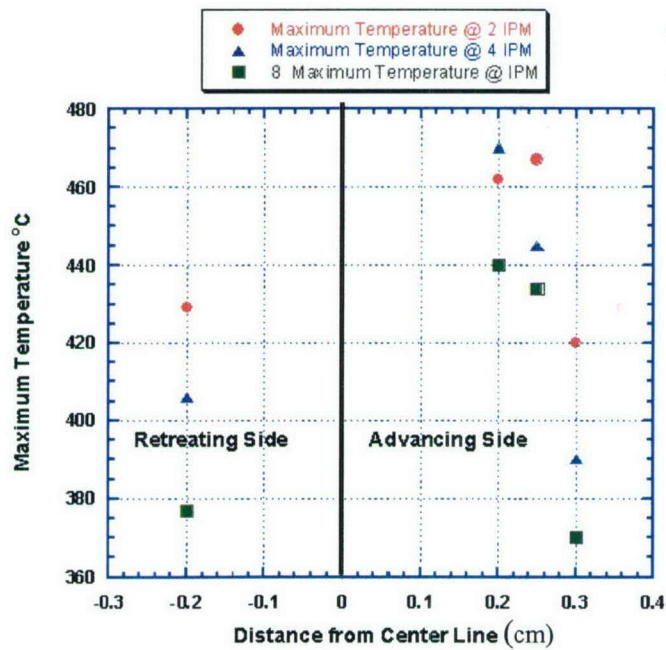


Figure 7. Mean maximum temperature (average of two measurements) recorded during FSW using a conventional tool. The travel speeds were 2, 4, and 8 inches per minute.

The microstructures of the nuggets produced by the three tool geometries are significantly different. A transverse view in the weld travel direction of the nugget produced by the conventional tool is a “squashed” ellipse (Figure 8a), that produced by the scroll shoulder tool has a truncated bell shape (Figure 8b), and that produced by the tri-flute tool is more like a circle (Figure 8c). The size of the nugget decreases at the faster travel speeds because the tool diameter traverses a point on the surface more quickly, allowing a lower heat input. The microstructure in the TMAZ varies with travel speed and tool geometry. The TMAZ, formed by the standard tool at the two slower travel speeds (2 and 4 ipm) and by the scroll shoulder tool at 2 ipm, has the parent grains deformed upward (Figure 9a), emerging at the surface. The TMAZ in the weld produced by the standard tool at 2 ipm and the scroll shoulder tool at a travel speed of 8 ipm and 16 ipm has the parent grains deformed downward (Figure 9b). The parent grains in the TMAZ formed by the tri-flute tool are deformed only slightly upward (Figure 9c).

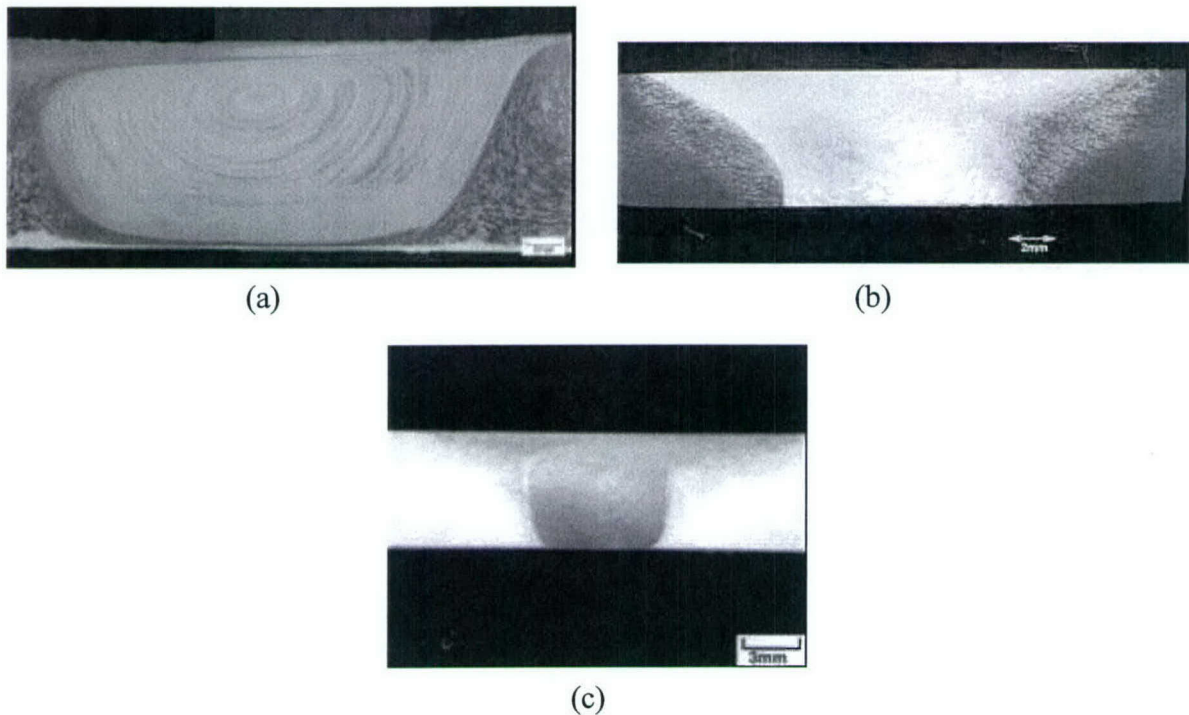


Figure 8. Cross sectional view of (a) the nugget in FSW AA7050-T7 produced by a conventional tool, (b) the nugget in FSW AA7050-T7 produced by a tool with a scroll shoulder, and (c) the nugget in FSW AA7050-T7 produced by tri-flute tool.

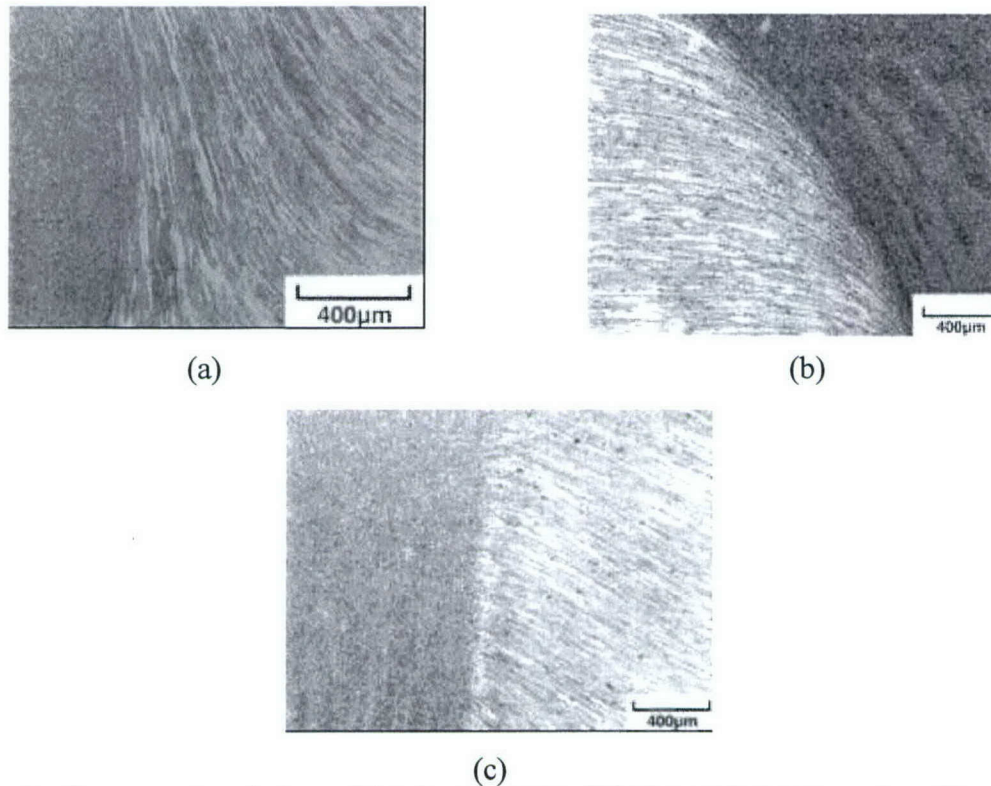


Figure 9. Cross sectional view of (a) the TMAZ in FSW AA7050-T7 produced by a conventional tool at a travel speed of 4 ipm, (b) the TMAZ in FSW AA7050-T7 produced by a tool with a scroll shoulder at a travel speed of 8 ipm, and (c) the nugget in FSW AA7050-T7 and (c) the nugget in FSW AA7050-T7 produced by tri-flute tool.

Stress Corrosion Cracking Test Results

Standard Tool

Figure 10 compares the strain rate dependence of the elongation in SSR specimens from FSW AA 7050-T7651 joined using a conventional tool at travel velocities of 2 ipm with those joined at travel velocities of 4 ipm. The ductility and elongation at the highest strain rate, $3 \times 10^{-4} \text{ s}^{-1}$, were the same as that in air. This indicates that crack growth at the fastest strain rate used in the SSR tests was too rapid for the environment to exert effects on the crack growth rate. The elongation of specimens made from the material joined at a travel velocity of 4 ipm decreased, due to SCC, over 200% at a strain rate of $3 \times 10^{-5} \text{ s}^{-1}$ relative to those tested at $3 \times 10^{-4} \text{ s}^{-1}$. Whereas, there was little change in the elongation in specimens from the material joined using the conventional tool at a travel velocity of 2 ipm until the strain rate was $< 3 \times 10^{-6} \text{ s}^{-1}$. The strain rate dependence on the elongation of the material joined at a travel speed of 8 ipm was very similar to that joined at 4 ipm.

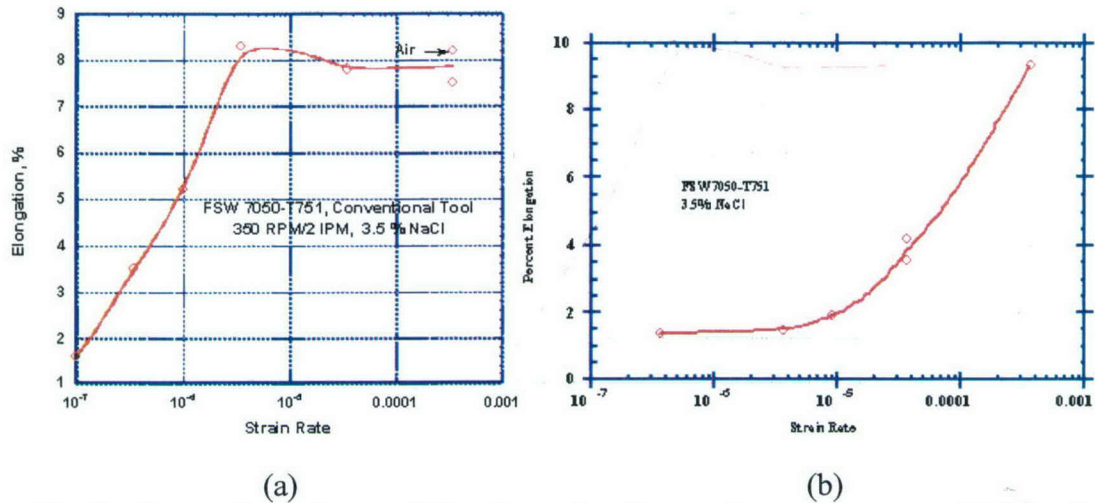


Figure 10. Strain rate dependence of the elongation for specimens from material joined by the conventional tool at travel speeds of (a) 2 ipm and (b) 4 ipm and tested in 3.5% NaCl solution, showing the better SCC resistance of the 2 ipm specimens.

Microscopy on the failed SSR specimens, joined using the standard tool, showed that the location and nature of the fracture changed when SCC caused a loss of ductility. All specimens tested that failed with no loss or slight loss in ductility, relative to failure in air, fractured approximately 8mm distance from the weld nugget. The fracture path was located in the large grain region within the HAZ and was transgranular. Figure 11 is a typical example of a specimen that failed in this manner. This is a specimen from the material joined using the standard tool at a travel speed of 2 ipm. It was pulled to failure at a strain rate of $3 \times 10^{-6} \text{ s}^{-1}$. The shoulder at the bottom of the macrograph indicates that the failure occurred on the advancing side. The necking in the optical cross sectional view of Figure 11a as well as the SEM fractograph shown in Figure 11b indicates that the fracture is ductile, although there are a few highly dispersed "groves" in the SEM fractograph apparently where intergranular SCC has occurred, i.e. the pancake-like grains have been pulled out. When the strain rate was reduced by a factor of three to $1 \times 10^{-6} \text{ s}^{-1}$ or less, the fracture shifted to the nugget side of the TMAZ/nugget interface (Figure 12a). SEM fractography (Figure 12b) also shows that the fracture is intergranular and through the equiaxed fine recrystallized grains of the nugget. For specimens from material joined by the standard tool at a travel speed of 4 ipm, intergranular SCC occurred on the nugget side at the TMAZ/nugget interface in all SSR specimens, from samples tested at strain rates slower than $3 \times 10^{-4} \text{ s}^{-1}$.

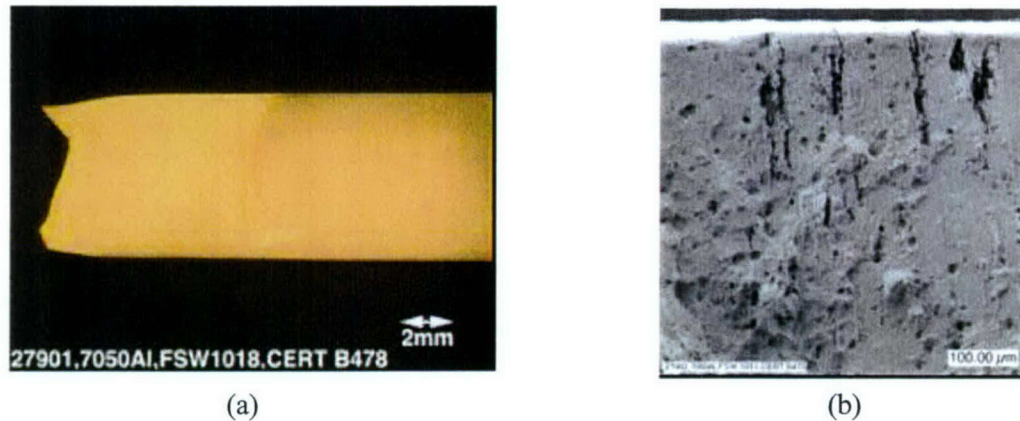


Figure 11. Ductile failure in a SSR specimen (standard tool 2 ipm) tested in 3.5% NaCl solution at a strain rate of $3 \times 10^{-6} \text{ s}^{-1}$ (a) optical macrograph (b) SEM fractograph.

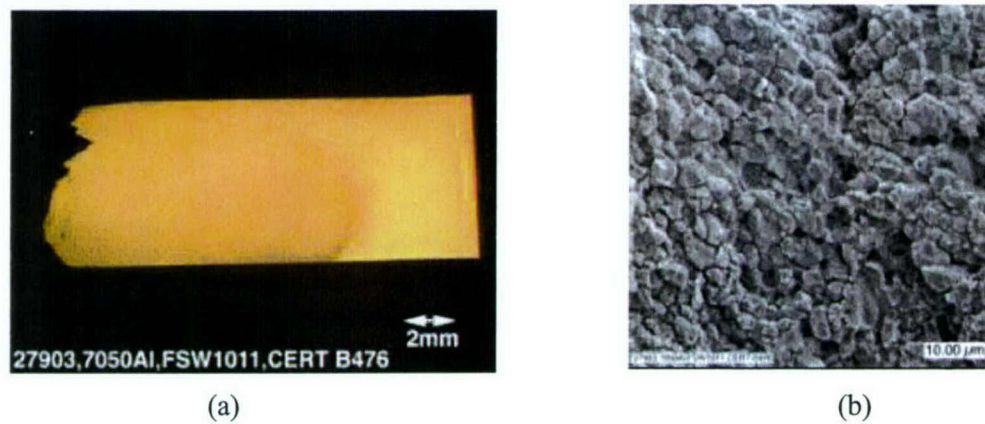


Figure 12. Intergranular SCC failure in a SSR specimen (standard tool 4 ipm) tested in 3.5% NaCl solution at a strain rate of $1 \times 10^{-6} \text{ s}^{-1}$ (a) optical macrograph (b) SEM fractograph.

Scroll Shoulder Tool

Table 1 shows the SSR results for the FSW AA 7050-T7651 joined using the scroll shoulder tool at the various travel speeds. The table compares the elongation in air and in 3.5% NaCl at a strain rate of $3 \times 10^{-6} \text{ s}^{-1}$. There is a significant decrease in the elongation in solution, relative to air, (loss of ductility) in the specimen that had been joined at a travel speed of 2 ipm. There is no change in the elongation in air and in solution in the specimen from material joined at 16 ipm. The elongation in solution of the material joined at 8 ipm is intermediate to that of material joined at 2 ipm and 16 ipm. Thus, the effects of tool travel speed of the standard tool and the scroll shoulder tool on the SCC resistance of FSW AA 7050-T7651 go in the reverse directions for the two tools, i.e. increased heat input degrades the SCC resistance of material joined using the scroll shoulder tool and increases the SCC resistance of the material joined by the standard tool. Figure 13 is the strain rate dependence for the material joined at 8 ipm. There is little loss in ductility until the strain rate is less than $1 \times 10^{-6} \text{ s}^{-1}$. This indicates that the SCC

crack growth rate is slower in the AA 7050-T7651 material joined using the scroll shoulder tool at a travel speed of 8 ipm than that joined by any travel speed by the standeard tool.

Microscopy of the SSR test specimens from the material joined using the scroll shoulder tool showed that the fractures in air were ductile as were the fractures in specimens from the material joined at a travel speed of 16 imp in Table 1 that were tested in solution. The failures of the material joined at a travel speed 8 ipm and tested at strain rates of $1 \times 10^{-6} \text{ s}^{-1}$ or higher in solution (Figure 13) also failed by a transgranular ductile mode in a large grain region within the HAZ. The optical cross sectional view and the SEM fractography looked like that in Figure 11. In contrast, the SSR samples from material joined at a travel speed of 8 ipm and tested in solution at strain rates $< 1 \times 10^{-6} \text{ s}^{-1}$ failed by intergranular SCC in the HAZ on the retreating side of the nugget, Figure 14. The same type of failure occurred in the specimen from material joined at 2 ipm and tested in solution at a strain rate of 3.5×10^{-6} , Table 1. The specimens from material joined using the scroll shoulder tool are the only FSW AA 7050-T7651 that did not have an SCC failure at the nugget/TMAZ interface.

Table 1. SSR results for FSW AA7050-T7651 joined using the scroll shoulder tool at different travel speeds.

	Air/ ($3.5e^{-4}$)		3% NaCl/ ($3.5e^{-6}$)	
	ksi UTS	% Elongation	ksi UTS	% Elongation
350 RPM/2 IPM	54.6	6.9	46.3	3.1
350 RPM/8 IPM	60.7	7.4	64.1	6.4
350 RPM/16 IPM	62.5	10.3	65.0	10.1

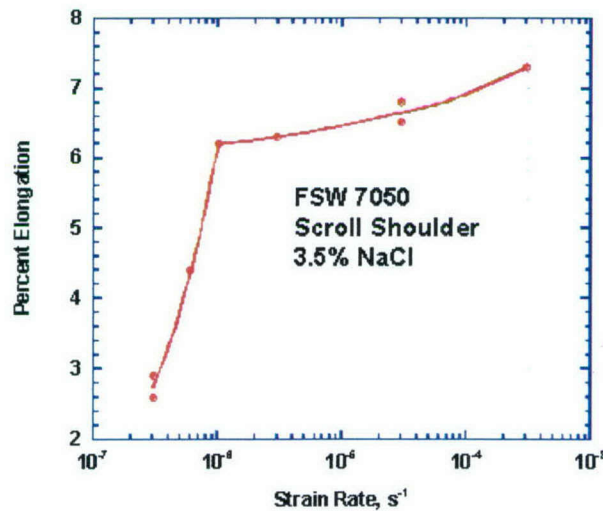


Figure 13. Strain rate dependence of the elongation for specimens from material joined by the scroll shoulder tool at a travel speed of 8 ipm and tested in a 3.5% NaCl solution.

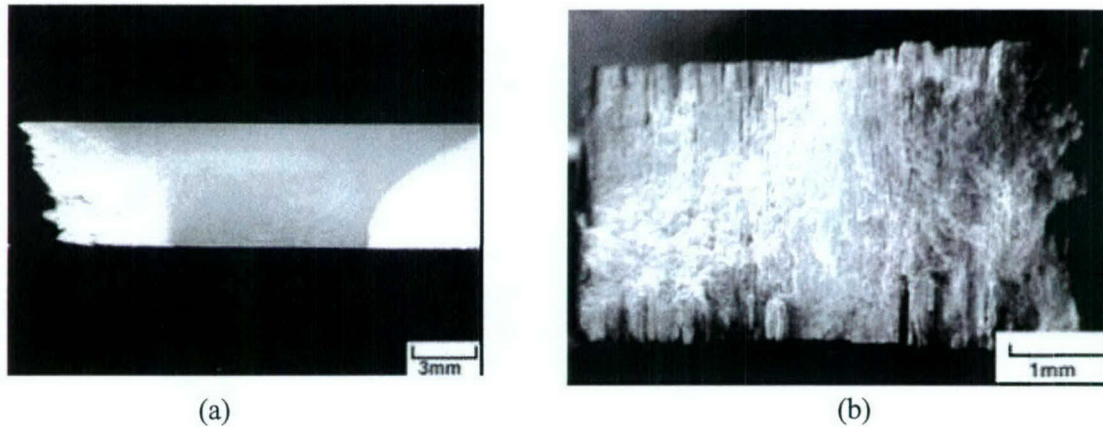


Figure 14. Intergranular SCC failure in a SSR specimen from material joined at 8 ipm using the scroll shoulder tool and tested in 3.5% NaCl solution at a strain rate of $1 \times 10^{-6} \text{ s}^{-1}$ (a) optical macrograph (b) SEM fractograph.

Tri-Flute Tool

The third type of tool geometry, flat shoulder with a tri-flute pin, was used at one travel speed (4 ipm) to join material. The SSR results for the strain rate dependence of the elongation for this material are shown in Figure 15. These results are almost identical to those of the material joined by the standard tool at a travel speed of 4 ipm at strain rates below $3 \times 10^{-5} \text{ s}^{-1}$. The SSR results differ at the strain rate $3 \times 10^{-5} \text{ s}^{-1}$ where the material joined by the standard tool has lost most of its ductility, but the material joined by the tri-flute tool has almost the same elongation as that at $3 \times 10^{-4} \text{ s}^{-1}$. The elongation in solution at the $3 \times 10^{-4} \text{ s}^{-1}$ strain rate is the same elongation as that in air. Microscopy showed that the fracture behavior of the material joined using the tri-flute tool was the same as that observed for material joined using the standard tool, i.e. ductile failure occurred at the strain rates that had high elongations and intergranular failure on the nugget side of the TMAZ/nugget interface.

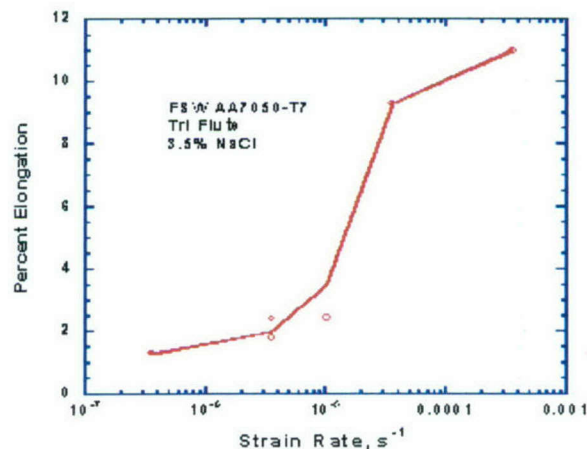


Figure 15. Strain rate dependence of the elongation for specimens from material joined by the tri-flute tool at a travel speed of 4 ipm and tested in a 3.5% NaCl solution.

TEM Results

Grain Size

A transmission electron microscopy (TEM) study was undertaken to evaluate any differences in the microstructure and/or chemistry between the region most susceptible to corrosion (SCC) and other regions, including the parent metal. The microstructural features of interest included grain sizes, grain boundary precipitation, and matrix precipitation. The FSW AA 7050 material analyzed had been joined using the standard tool at a travel speed of 4 ipm, where SCC failure occurred on the nugget side of the TMAZ/nugget interface. Figure 16 shows the recrystallized grains in the nugget and compares them with the elongated pancake microstructure of the parent material. The grain sizes of the four regions are listed in Table 2. In those regions affected by the stirring action, the grains are equiaxed (recrystallized), whereas, in the base metal, grains are elongated. There is no direct correlation of grain size with corrosion susceptibility.

Table 2. Grain size in the various weld zones.

Region	Grain Size, μm
Nugget, center	3 - 5
Nugget, at TMAZ	2 - 3
TMAZ, at nugget	1 - 2
TMAZ, advancing side	4 - 10
TMAZ, trailing side	5 - 10
Base Metal	Approx. 1 wide > 10 long

Matrix Precipitation

Moving from the hottest region of the weld zone (the center of the nugget) to the coolest region (the TMAZ) there is an increasing amount of matrix precipitation, Figure 17. There are two populations of precipitates. The larger angular $\text{Mg}(\text{Zn}_2\text{AlCu})$ and the finer Al_3Zr . There are fewer of the larger precipitates in the TMAZ than in the nugget. The finer particles are spheroidal in the nugget and ellipsoidal in the TMAZ and are much more prevalent in the TMAZ. There does not appear to be a direct correlation between abundance or distribution of the matrix precipitates and susceptibility to corrosion.

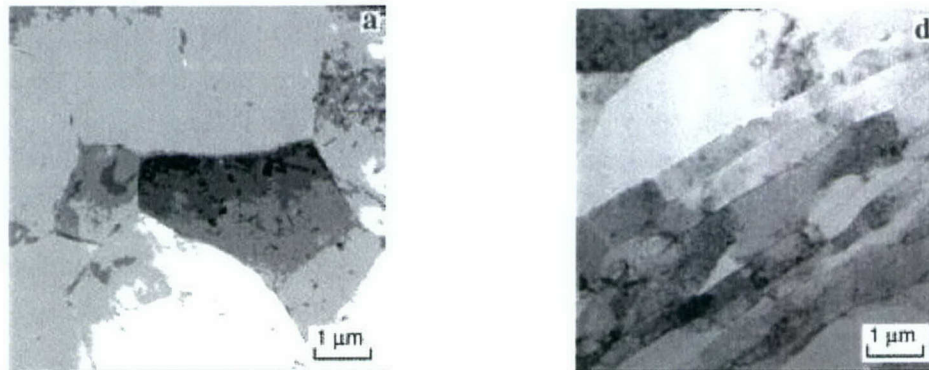


Figure 16. Comparison of grain size in FSW AA7050 in the (a) nugget and (b) parent material.

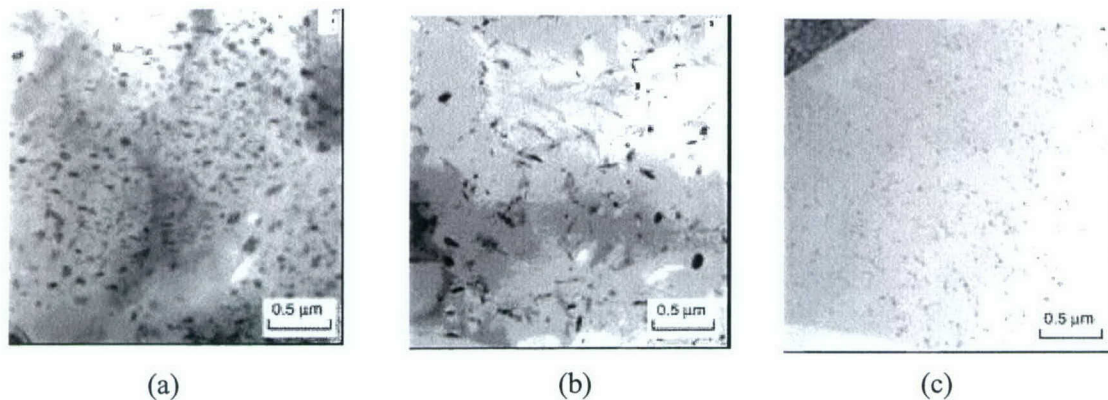


Figure 17. Comparison of the size of precipitates in FSW AA7050 in the (a) nugget, (b) TMAZ, and (c) parent material.

Grain Boundary Precipitation

The grain boundary particles have roughly the same composition as the larger matrix precipitates, $Mg(Zn_2AlCu)$. There is not a large difference in the distribution of grain boundary particles across the nugget. The grain boundary particles in the TMAZ are smaller than in the nugget, likely because the temperature in the TMAZ was less than that in the nugget.

X-ray energy dispersive spectroscopy (EDS) was used to measure compositions at various positions within the nugget and TMAZ microstructure. Results obtained are shown in Tables 3-5. Because the analysis cross section of the beam is approximately 40 nm, measurements include matrix material adjacent to the boundary. Thus, the absolute values will be skewed by the matrix composition. For this reason measurements are also reported as ratios of Zn, Mg, and Cu as well as absolute values. The microstructures analyzed include grain boundaries with no particles (clean boundaries), grain boundaries near particles, and in the matrix adjacent to the particles.

The so-called “clean grain boundaries”, i.e., those without obvious precipitates were fairly rare in both the advancing side and the trailing side of the TMAZ. One would expect that grain boundaries without precipitation would have a composition reflecting the alloy composition (Al - 2.7Zn - 2.6Mg - 1.0Cu). Since there is generally less of each of these elements in these boundaries, Table 3, this suggests that the “clean boundaries” may be segments of boundaries in which $Mg(Zn_2AlCu)$ particles have precipitated, but which have been polished away during foil preparation.

Examination of the boundaries near $Mg(Zn_2AlCu)$ particles reveals a diminished concentration of Cu, Mg, and Zn, Table 4, like the “clean boundaries”. Mg appears to be the most variable of the elements analyzed. It is not clear from Tables 2 and 3 that any one of the elements analyzed is responsible for the increased corrosion susceptibility of the most sensitized region boundaries in the nugget at the TMAZ. However, this region does have the lowest Mg contents. But it is important to note that the whole weld zone is sensitized and susceptible to intergranular corrosion, and that all regions of the weld zone examined had diminished Mg and Zn contents, relative to the bulk alloy level.

Interiors of the grains were examined also. In this case, the matrix, in which the fine precipitates were distributed, was analyzed, Table 5. This composition can be compared to the grain boundary compositions reported in table 2 and 3 to provide some insight as to why corrosion might occur at, or near grain boundaries. The relative Cu/Mg ratio is high as in the most susceptible boundary, but the Cu/Zn is low. Thus, it is not clear what grain boundary composition is responsible for the increased corrosion susceptibility.

Table 3. Composition of grain boundaries without particles.

Region of FSW 7050	Cu, a/o	Mg, a/o	Zn, a/o	Zn/Mg	Cu/Zn	Cu/Mg
Center of Nugget	0.5	2.3	3.0	1.4	0.17	0.25
Nugget, at TMAZ	1.0	1.2	1.8	1.5	0.56	0.83
TMAZ at Nugget	1.0	0	1.8	-	0.56	-
TMAZ, advancing side	1.1	1.2	1.7	1.4	0.65	0.92
TMAZ, trailing side	0.8	2.4	2.6	1.1	0.31	0.33
Base Metal	1.1	0.3	1.8	6	0.61	3.8

Table 4. Composition of grain boundaries near particles

Region of FSW 7050	Cu, a/o	Mg, a/o	Zn, a/o	Zn/Mg	Cu/Zn	Cu/Mg
Center of Nugget	0.8	1.8	2.5	1.4	0.32	0.44
Nugget, at TMAZ	0.7	0.8	1.7	2.1	0.41	0.88
TMAZ, at nugget	0.9	0.6	2.3	3.83	0.39	1.5
TMAZ, advancing side	0.8	1.8	2.2	0.82	0.36	0.44
TMAZ, trailing side	0.8	2.3	2.4	1.0	0.33	0.35
Base Metal	0.9	0	0.5	-	1.8	-

Table 5. Composition of matrix away from particles

Region of FSW 7050	Cu, a/o	Mg, a/o	Zn, a/o	Zn/Mg	Cu/Zn	Cu/Mg
Center of Nugget	0.9	2.9	3.1	1.1	0.29	0.31
Nugget, at TMAZ	1.1	0.7	2.8	4	0.39	1.6
TMAZ, at nugget	1.3	2.6	2.0	0.77	0.65	0.5
TMAZ, advancing side	1.2	4.0	2.5	0.63	0.48	0.3
TMAZ, trailing side	2.1	2.4	2.5	1.0	0.84	0.88

Pre/post weld heat treatment

The material used to investigate pre/post weld heat treatment was ¼ inch- thick AA7075-T7651 plates. The AA7075-T7651 was given a pre-weld solution anneal before FSW. Samples were welded using conventional friction stir welding practices of 4 ipm at 350 rpm [1]. The as-welded, solution annealed AA7075 material was then given conventional tempering treatments before corrosion testing: T-6 (121°C/24 hours), T73 (107°C/7 hours + 325°C/16 hours), and T76 (121°C /15 hours + 163°C/16 hours). A second set of solution annealed AA7075-T751 material was given the pre-weld thermal treatment of 107°C for 7 hours (This is the first stage of the two-stage T-73 temper). After samples were given the 107°C/7 hour thermal treatment, they were friction stir welded. The FSW samples were then given the tempering treatments 121°C for 24 hours (T-6), 163°C for 27 hours (second stage of T-73), and 163°C for 16 hours (second stage of T-76).

The macrographs in Figure 18 show the extent of intergranular attack on the as-welded AA7075-T7651 and the as-welded + thermally treated FSW AA7075 material after a six hour exposure in the modified EXCO solution. The attack on the FSW solution annealed material + T6 temper was the most severe of the post-weld thermally treated materials. The attack was greater in depth and as pervasive than that on the as-welded T76 specimen. The attack was least severe on the FSW solution annealed material + T76 temper. The material given the T73 past-weld temper was unique in that attack occurred both in the nugget and some distance beyond the nugget but showed a corrosion resistant zone adjacent to the nugget.

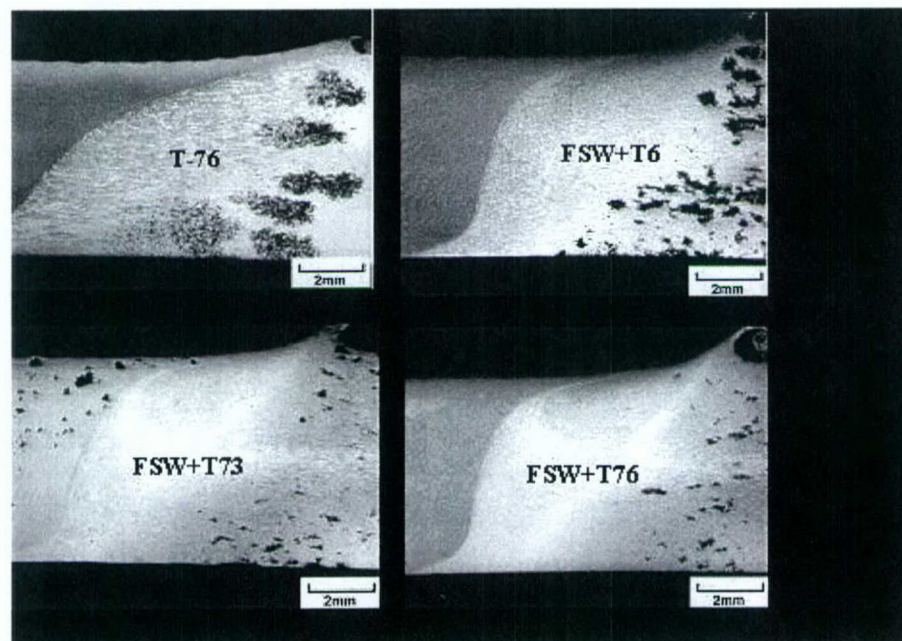


Figure 18. Intergranular corrosion attack after immersion for 6 hours in a modified EXCO solution (a) as welded AA7075-T7651, (b) welded solution annealed AA7075-T7651 + T6 (c) welded solution annealed AA7075-T7651 + T73, (d) welded solution annealed AA7075-T7651 + T76.

Figure 19 is a set of macrographs showing the attack resulting from immersion of the material that was given a pre weld temper of 107°C for 7 hours and then, after FSW, the post weld tempers: 121°C/24 hours, 163°C/27 hours, and 163°C 16 hours and compares the attack with that of as-welded FSW 7075-T76. The most heavily sensitized was the material given the 121°C/24 hour post weld temper. This is not a surprise since the post weld thermal treatment is the peak age T6 temper, which is the temper in commercial alloys producing high susceptibility to SCC. The materials given the post weld 163°C/27 hours and 163°C/17 hours tempers were the least attacked of all of the materials. These materials had only a few pits in the heat affected zones.

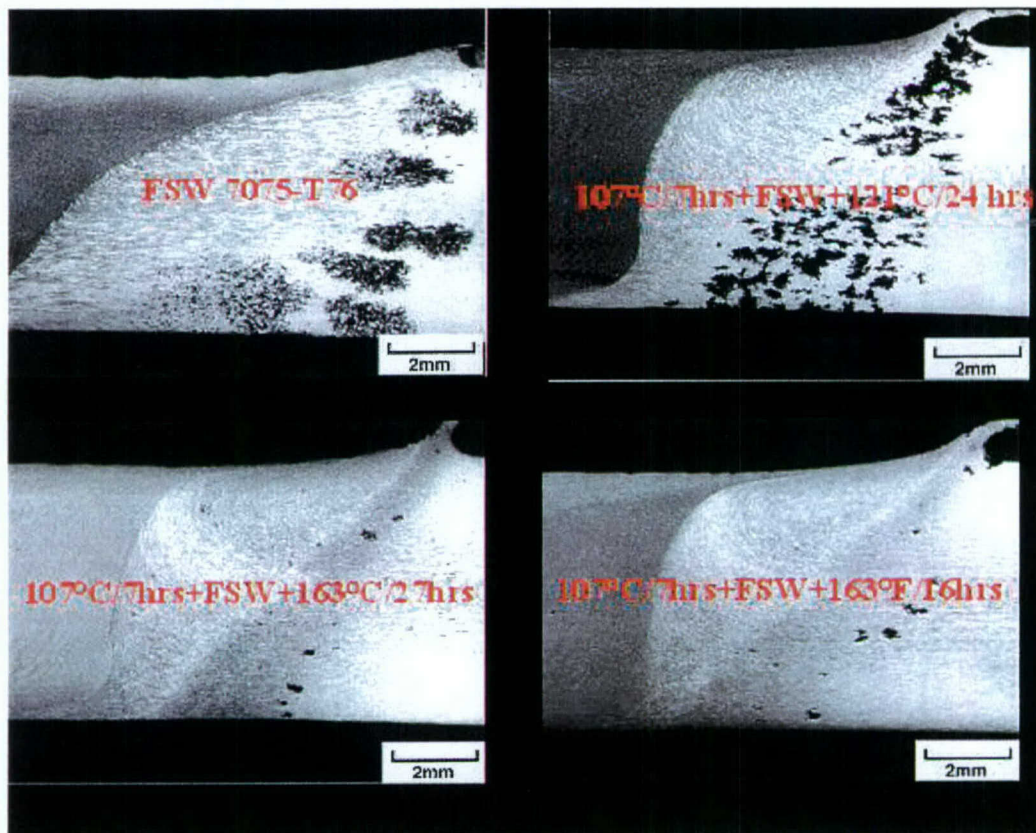


Figure 19. Intergranular corrosion attack after immersion for 6 hours in a modified EXCO solution in (a) as welded AA7075-T7651 and solution annealed AA7075-T7651 with a pre weld temper of 107°C/7 hours and post weld tempers (b) 121°C/24 hours, (c) 163°C/27 hours, and (d) 163°C/17 hours.

Table 6 gives the SSR results for AA7075 specimens in air and exposed to 0.6M NaCl while being tested at a strain rate of 10^{-6} s^{-1} . The table shows the strain to failure and the ultimate strength in air as well as the ratio of the strain to failure in solution to the strain to failure in air, which is referred to as the ductility ratio. The ductility ratio of the AA7075-T7651 parent material is near one, suggesting no susceptibility to SCC. The ductility ratio for as-welded FSW AA7075-T7651 is 0.64, indicating susceptibility to SCC. Of the six temper conditions, the T76 post weld temper and the two pre/post weld

tempers with the final temper temperature of 163°C had the highest ductility ratios, approximately 0.8. The materials with the T6 and T73 post weld temper had the lowest ductility ratio, 0.46. The SSR results followed the same trends as the immersion tests.

Table 1. Ultimate strength, strain to failure in air, and the ductility ratio in 0.6M NaCl for the parent material, naturally aged, and artificially aged FSW 7075-T7651 tested at a slow strain rate (10^{-6}s^{-1}).

	Air Strain to Failure %	Air Ultimate Strength (MPa)	Ductility Ratio $\epsilon_{\text{solution}}/\epsilon_{\text{air}}$
7075-T7651 (Parent)	10.4	532	0.95
FSW 7075-T7651 (Natural Age 5 mos.)	6.1	473	0.64
7075-Solution Treat + FSW + T6	6.1	364	0.46
7075-Solution Treat + FSW + T76	6.1	349	0.84
7075-Solution Treat + FSW + T73	6.1	357	0.46
7075-Solution Treat + 121°C/7 hrs + FSW + 121°C/24 hrs	4.9	428	0.65
7075-Solution Treat + 121°C/7 hrs + FSW + 163°C/27 hrs	4.0	373	0.77
7075-Solution Treat + 121°C/7 hrs + FSW + 163°C/17 hrs	3.7	347	0.80

Figure 20 shows microscopy of the SCC fracture in the SSR specimen from the material that was given the T76 post weld temper. This material had a ductility ratio of 0.84. The failure was located in the large grain region within the HAZ. There were some shallow intergranular penetrations on the edges, but the failure was mostly ductile. These microscopy results are typical for the material that had ductility ratios of approximately 0.8. Specimens with more rapidly propagating SCC cracks, those have ductility ratios between 0.64 and 0.46, had deeper intergranular penetrations (Figure 21). These longer intergranular cracks indicated a more rapid SCC crack growth rate than in the specimens with 0.8 ductility ratios. In both cases intergranular SCC cracks propagated from the sides of the specimen until the reduced load carrying cross section failed by ductile overload.

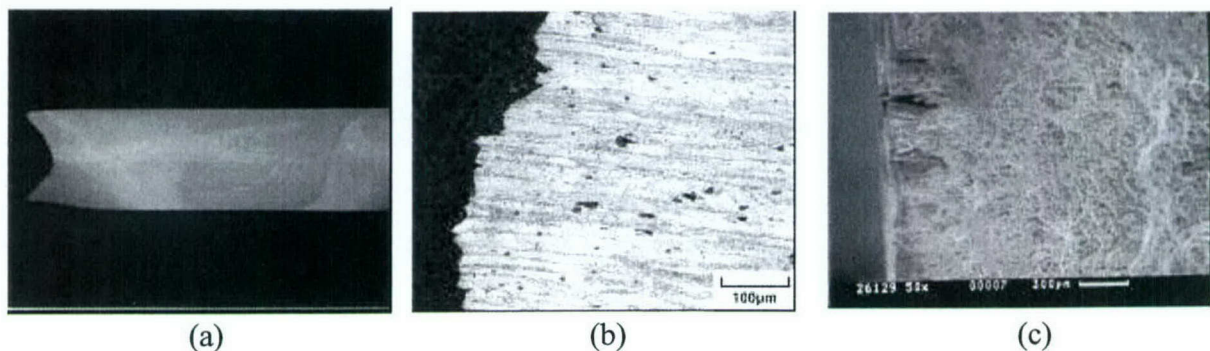
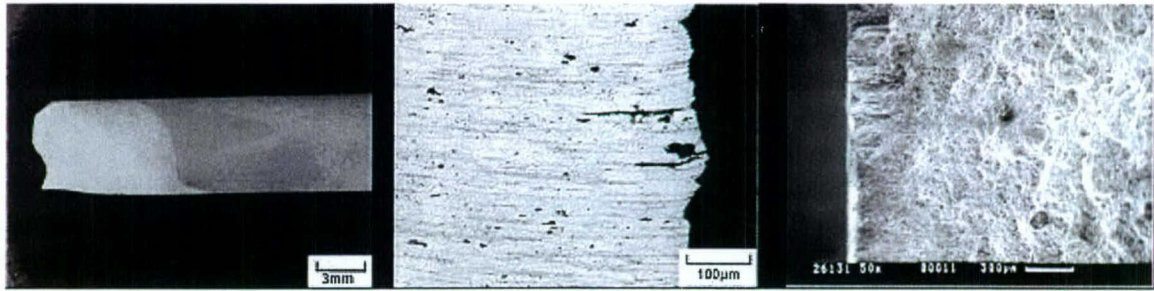


Figure 20. SCC fracture from SSR test of an AA7075 specimen that was solution treated before FSW and then given the T76 temper. (a) macrograph of cross section, (b) optical micrograph of the fracture path, and (c) SEM micrograph of the fracture face.



(a) (b) (c)

Figure 21. SCC fracture from SSR test of a AA7075 specimen that was solution treated and tempered at 121°C for 7 hours before FSW and then tempered at 121°C for 24 hours after FSW. (a) macrograph of cross section, (b) optical micrograph of the fracture path, and (c) SEM micrograph of the fracture face.

Transmission electron microscopy (TEM) measurements of grain boundary compositions were made via energy dispersive (x-ray) spectroscopy (EDS). The electron beam exciting the X-rays was position between the intermetallic precipitates in the boundaries. Although the electron probe was approximately 4nm in diameter, the spatial resolution likely approaches 40nm because of electron scattering by the alloy matrix. Since the precipitate spacing was in excess of 100nm, none of the detected x-rays originated from the intermetallics. Figure 22 gives summaries the grain boundary analysis, where each point is the average of 5 measurements. The three conditions exhibiting the best SCC resistance, with R-ratios of 0.84, 0.80, and 0.77, are grouped at the lower values for Zn and Mg, although they do not fall on a linear plot. The results for Cu suggest that the Cu level has no effect on the SCC susceptibility.

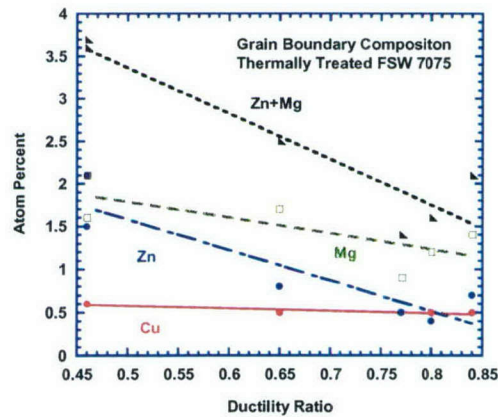


Figure 22. Influence of grain boundary composition of Cu, Zn, and Mg on the SCC resistance FSW AA7075.

SUMMARY

FSW sensitizes the microstructures of 7XXX high strength Al alloys to corrosion. The degree of sensitization and the location of the sensitized region in the weld zones are not predictable from the properties of the parent material. This program has examined five countermeasures. All except two are either ineffective or marginally effective. Post weld heat treatments were found that restore over 80% of the SCC resistance to the susceptible weld zone, but at a loss of strength. Altering the tool design from the standard flat shoulder tri flat threaded pin to a scroll shoulder-tri flat threaded pin with an optimized travel speed was found to significantly increase the SCC resistance. Thermocouple measurements showed that the peak temperatures in the weld zone were approximately 40°C less at corresponding locations for the scroll shoulder tool relative to the standard tool. A TEM evaluation could find no difference in grain size, precipitate distribution, and precipitate composition between weld zones that were highly susceptible to SCC and those that were more resistant to SCC. A comparison of grain boundary compositions of the weld zones in FSW 7050-T7 and post weld heat treated FSW 7075 specimens indicated that the relationship between grain boundary composition and susceptibility to SCC is a complex one. The sensitized boundaries in FSW 7050-T7 are depleted in Mg and Zn relative to the bulk composition; whereas, SCC resistance in post weld heat treated FSW 7075 increases as the Mg and Zn concentration in the boundaries increases.

REFERENCES

1. W.M. Thomas, et al, "Friction Stir Butt Welding", International Patent Appl. No. PCT/GB92/02203, GB Patent Appl. No. 9125978.8, Dec. 1991, and U.S. Patent No. 5,460,317, (Oct. 24, 1995).
2. C.J. Dawes and W.M. Thomas, *TWI Bulletin* 6, 124 (Nov./Dec. 1995).
3. M. Ellis and M. Strangwood, *TWI Bulletin* 6, 138 (Nov/Dec 1995).5 C.J. Dawes and W.M. Thomas, *Welding Journal*, 75 (3), 41 (1996).
4. O.T. Midling, "Material Flow Behavior and Microstructural Integrity of Friction Stir Butt Weldments", *Proc. 4th Int'l. Conf. on Aluminum Alloys*, Atlanta GA, (Sept. 1994).
5. M.W. Mahoney, *Welding and Joining*, pp. 18-20, (Jan./Feb. 1997).
6. S. Kallee and D. Nicholas, *Welding and Joining*, pp.18-21, ((Feb. 1998).
7. C. J. Dawes, *Welding & Metal Fabrication*, pp.14-16, (January 1995).
8. J. B. Lumsden, M.W. Mahoney, G. Pollock, D. Waldron, and A. Guinasso, *Proceedings First International Symposium on Friction Stir Welding*, 14-16 June 1999, Thousand Oaks, CA.

9. J. B. Lumsden, M. W. Mahoney, and C. G. Rhodes, "Intergranular Corrosion Following Friction Stir Welding of 7075-T6 Aluminum" *Corrosion*, 55 (1999), 69-74.
10. J. B. Lumsden, M. W. Mahoney, C. G. Rhodes, and G.A. Pollock, "Corrosion Behavior of FSW 7050-T7651" *Corrosion*, 59 (2003) 212-219.
11. J. Lumsden, G. Pollock, and M. Mahoney, "Effect of Post Weld Heat Treatments on the Corrosion Properties of FSW AA7050", *Friction Stir Welding and Processing II*, K. V. Jata, M. W. Mahoney, R. S. Mishra, S. L. Semiatin, T. Lenert, eds., TMS (2003) , p99.
12. Jesse Lumsden, Gary Pollock, and Murray Mahoney, "Friction Stir Weld Tool Design to Improve the Stress Corrosion Resistance of AA7050-T7", to be published in the Proc. *Friction Stir Welding and Processing IV*, TMS.
13. Jesse Lumsden, Gary Pollock, and Murray Mahoney, "The Effect of Thermal Treatment on the Corrosion Behavior of Friction Stir Welded 7050 and 7075 Aluminum Alloys" THERMEC, *Materials Science Forum* Vols. 426-432, (2003) p 2867.